

Dynamical rate equation model for femtosecond laser-induced breakdown in dielectricsJean-Luc Déziel,^{1,2} Louis J. Dubé,^{1,2,*} and Charles Varin^{1,3,4,†}¹*Département de physique, de génie physique et d'optique, Université Laval, Québec G1V 0A6, Canada*²*Centre interdisciplinaire en modélisation mathématique, Université Laval, Québec G1V 0A6, Canada*³*Département de physique, Cégep de l'Outaouais, Gatineau, Québec J8Y 6M4, Canada*⁴*Centre collégial de transfert de technologie en cybersécurité, Cégep de l'Outaouais, Gatineau, Québec J8Y 6M4, Canada*

(Received 19 June 2019; revised 18 March 2021; accepted 22 June 2021; published 6 July 2021)

Experimental and theoretical studies of laser-induced breakdown in dielectrics provide conflicting conclusions about the possibility to trigger ionization avalanche on the subpicosecond time scale and the relative importance of carrier-impact ionization over field ionization. On the one hand, current models based on a single ionization-rate equation do not account for the gradual heating of the charge carriers, which, for short laser pulses, might not be sufficient to start an avalanche. On the other hand, kinetic models based on microscopic collision probabilities have led to variable outcomes that do not necessarily match experimental observations as a whole. In this paper, we present a rate-equation model that accounts for the avalanche process phenomenologically by using an auxiliary differential equation to track the gradual heating of the charge carriers and define the collisional impact rate dynamically. The computational simplicity of this dynamical rate-equation model offers the flexibility to extract effective values from experimental data. This is demonstrated by matching the experimental scaling trends for the laser-induced damage threshold of several dielectric materials for pulse durations ranging from a few fs to a few ps. Through numerical analysis, we show that the proposed model gives results comparable to those obtained with multiple rate equations and identify potential advantages for the development of large-scale, three-dimensional electromagnetic methods for the modeling of laser-induced breakdown in transparent media.

DOI: [10.1103/PhysRevB.104.045201](https://doi.org/10.1103/PhysRevB.104.045201)**I. INTRODUCTION**

Computer modeling of strong-field optical phenomena in dielectrics driven by intense laser radiation is essential to understand the fundamental processes in play, e.g., during laser micromachining, laser surgery, and high-harmonic generation in solids, to name a few. Mechanisms for laser-induced breakdown were identified and studied in various contexts [1–12]. In the accepted picture, plasma formation in laser-driven dielectrics proceeds as follows. (i) Charge carriers are first created by field ionization (FI). (ii) The charge carriers absorb energy from the laser field [a process we generically refer to as laser heating (LH)]. (iii) The hot charge carriers create new, cold ones through collisional ionization (CI). (iv) The cold carriers created by CI in turn gain energy from the laser field and create new carriers, and so on. The multiplication of charge carriers in (ii)–(iv) leads to an exponential growth of the carrier density, often referred to as an ionization avalanche. This picture applies well when the avalanche sequence (LH-CI) has enough time to unfold, e.g., when the pulse duration is in the picosecond range or above. However, current experimental and theoretical studies of laser-induced breakdown in dielectrics provide conflicting conclusions about the relative importance of LH-CI over FI and the possibility to trigger

ionization avalanche on the subpicosecond time scale (compare, e.g., Refs. [13,14] or [15,16]).

We emphasize that FI and LH-CI are two different channels through which damage is potentially induced. Although, in certain ranges of pulse durations and laser intensities, FI or LH-CI may dominate, in general they both contribute in comparable proportions (see, e.g., Ref. [17]).

Effectively, laser-induced breakdown emerges as a complex interplay between optical and dynamical processes, both influenced by a wealth of microscopic phenomena. Conflicting interpretations are not surprising, provided that: (i) current and past experiments involve different measurement techniques, materials, and laser parameters, making direct comparison difficult; (ii) assessing laser-induced breakdown is a highly nonlinear, nonperturbative problem difficult to address both analytically and numerically; (iii) theoretical predictions typically rely on simplified models that may miss important dynamical contributions; and (iv) numerical analysis to predict the damage threshold is sensitive and inherently bound to steady-state microscopic parameters whose definition and value vary significantly across the literature and/or may be hard to determine experimentally/theoretically (e.g., through direct measurement or *ab initio* simulations).

A major challenge thus lies in the development of simplified theoretical models that can reproduce experimental observations reliably as a whole, without a *a priori* bias toward FI or avalanche (LH-CI). In this context, models based on ionization rates are appealing, as they offer the possibility to match experimental data with reasonable agreement using

*Louis.Dube@phy.ulaval.ca

†charles.varin@cegepoutaouais.qc.ca

effective parameters, without having to include the contributions from individual microscopic processes explicitly (see, e.g., Refs. [17,18]). However, current implementations of the avalanche process in rate-equation models rely on open sets of differential equations and microscopic probability parameters to define the LH and CI rates, which is not an ideal situation as stated in point (4) above. For example in Refs. [2,6,10,19], simulations were performed within similar theoretical frameworks, but led to conflicting conclusions as different values for the LH rates were used.

In this paper, we present a rate-equation model that accounts for the avalanche process (LH-CI) with a simpler mathematical approach than previous methods. By using an auxiliary differential equation to track the gradual LH of the charge carriers, it allows us to define the CI rate dynamically from the fraction of carriers whose kinetic energy is high enough to potentially create new carriers through CI. The computational simplicity of this dynamical rate equation (DRE) model offers the flexibility to extract effective values from experimental data. This will be demonstrated by matching the experimental scaling trends for the laser-induced damage threshold of several dielectric materials for pulse durations ranging from a few fs to a few ps. The numerical implementation of the proposed model gives results comparable to those obtained with multiple rate equations (see Secs. II B and IV) and highlights the potential advantages for the development of large-scale, three-dimensional electromagnetic methods for the modeling of laser-induced breakdown in transparent media.

The paper is organized as follows. First in Sec. II we present an overview of two popular rate-equation models. Next in Sec. III, we describe the proposed DRE model in details. In Sec. IV, numerical analysis is used to compare the three models presented in the previous sections. In Sec. V, the DRE model is used to fit experimental data and extract effective values for the damage threshold in several dielectric materials. In Sec. VI, we discuss some of the limitations of the DRE model and, ultimately, we conclude in Sec. VII. Appendixes gather some of the technical aspects of the model and of its implementation. All calculations were performed using a PYTHON package that we made available online [20].

II. OVERVIEW OF CURRENT RATE EQUATION MODELS FOR LASER-INDUCED PLASMA FORMATION IN DIELECTRICS

The modeling of the laser-induced polarization and breakdown dynamics in solid-state dielectrics typically involves three complementary ingredients: in a two-band perspective (i) the polarization dynamics from bound electrons; (ii) the free currents associated with the motion of holes and electrons in the valence and conduction bands; and finally, (iii) the dynamics of the valence and conduction bands populations (ionization and recombination). Rigorous treatment would rely, e.g., on the semiconductor Bloch equations [18,21,22]. However, a split-model approach based on rate equations for the band population dynamics coupled with models for bound (e.g., Lorentz) and free (e.g., Drude) currents effectively provides a fair, phenomenological description of laser-induced breakdown on a cycle-averaged, statistical level (see, e.g.,

Ref. [17]). This simplified and intuitive approach is widely used in plasma physics for instance, as it offers both modeling flexibility and simplicity (see, e.g., Refs. [15,23,24]). For examples of bound and free currents models see, e.g., Refs. [17,22,25–27]. Next, we give an overview of two popular and established rate-equation models for the band-population dynamics.

A. Single rate equation

The single rate equation (SRE) model offers a phenomenological description of the band-population dynamics in dielectrics driven by intense laser light. It is characterized by an equation of the following form (see, e.g., Refs. [15,17,18,23]):

$$\frac{d\rho}{dt} = W \underbrace{\frac{\rho_u}{\rho_{\text{mat}}}}_{\text{FI}} + \alpha \rho I \underbrace{\frac{\rho_u}{\rho_{\text{mat}}}}_{\text{CI}} - \underbrace{\gamma_r \rho}_{\text{REC}}, \quad (1)$$

where ρ is the charge-carrier number density. The first term on the right-hand side is associated with field ionization (FI) at a rate $\nu_{\text{fi}} = W/\rho_{\text{mat}}$, where ρ_{mat} is the material number density. The intensity-dependent density-rate W is typically calculated using the Keldysh theory [28] or recent improvements [18,29–31] (see also Appendix A). The second term is associated with collisional ionization (CI) at a density-rate $\alpha \rho I$, where α is the impact rate coefficient, and $I = c\epsilon_0 n_0 E^2/2$ is the laser intensity, with E being the amplitude of the electric field, n_0 the linear refractive index of the dielectric material, c the speed of light *in vacuo*, and ϵ_0 the electric constant. Finally, the last term of Eq. (1) accounts for the spontaneous recombination (REC) at a rate γ_r .

In the formulation above, FI and CI are weighted by the fraction of unionized material ρ_u/ρ_{mat} , where $\rho_u = \rho_{\text{mat}} - \rho$, to include saturation of ionization (if we account for single ionization at most). Typically, during laser-induced breakdown the carrier density ρ remains small compared with the material density ρ_{mat} , i.e., $\rho_u/\rho_{\text{mat}} \simeq 1$. As a result, this weighting factor is often omitted (see, e.g., Refs. [18]). In this paper, we keep ρ_u to ensure a proper link to other models [see, in particular, Eq. (10)].

In Eq. (1), the CI rate is proportional to the carrier density ρ , which implies that all charge carriers can contribute to CI, regardless of their energy. This causes an overestimation of CI, especially at low fluence. This intrinsic bias can be partly compensated by an effective value for the impact rate coefficient α . However, a better strategy is to improve SRE to account for the gradual heating of the carriers until they absorb enough energy from the laser field to bring new electrons above the band gap. The multiple rate equations (MRE) (see Sec. II B) and the dynamical rate equation (DRE) (see Sec. III) models address this issue, although with somewhat different emphasis.

B. Multiple rate equations

The multiple rate equations (MRE) model implements laser heating (LH) and subsequent collisional ionization (CI) by using auxiliary differential equations to track the energy distribution of the electrons in the conduction band [2,32].

Effectively, an electron needs to acquire a minimum energy \mathcal{E}_c to be able to bring a new valence electron across the band gap to the conduction band. To respect both energy and momentum conservation, this critical kinetic energy is [1]

$$\mathcal{E}_c = \left(1 + \frac{m_r}{m_h}\right)(\mathcal{E}_g + \mathcal{E}_p), \quad (2)$$

where $m_r^{-1} = m_e^{-1} + m_h^{-1}$ is the reduced mass, m_e is the effective electron mass, m_h is the effective hole mass, \mathcal{E}_g is the band gap energy and \mathcal{E}_p is the ponderomotive energy. (See Appendix B for the definition of \mathcal{E}_p).

Technically, MRE includes the LH-CI sequence by discretizing the energy distribution in $k + 1$ energy levels, where $k = \lceil \mathcal{E}_c / \hbar\omega \rceil$, such that the upper level k sits above \mathcal{E}_c (the counting starts at 0). These levels are separated by increments of photon energy $\hbar\omega$ and associated with an individual population such that:

$$\rho = \sum_{j=0}^k \rho_j. \quad (3)$$

The following rate equations for the level densities are then solved:

$$\frac{d\rho_0}{dt} = \nu_{fi}\rho_u - \gamma_{th}\rho_0 + 2\gamma_u\rho_k - \gamma_r\rho_0, \quad (4a)$$

⋮

$$\frac{d\rho_j}{dt} = \gamma_{th}(\rho_{j-1} - \rho_j) - \gamma_r\rho_j; \quad \text{for } 1 \leq j < k, \quad (4b)$$

⋮

$$\frac{d\rho_k}{dt} = \gamma_{th}\rho_{k-1} - \gamma_u\rho_k - \gamma_r\rho_k. \quad (4c)$$

This set of coupled equations is interpreted as follows. First, the population of the zeroth level ρ_0 (the bottom of the conduction band) is seeded by FI [the first term on the right-hand side of Eq. (4a)]. As electrons absorb photons at a rate γ_{th} , they pass to the next level, as described by Eq. (4b). After having absorbed k photons, some electrons reach the upper level k , above the critical energy \mathcal{E}_c , defined by Eq. (2). At this level, laser heating is artificially stopped to limit the number of rate equations. From then on, electrons can collide with neutral, unionized material and cause CI events at a rate γ_u [see Eq. (10) for definition]. They then lose their kinetic energy and fall back to the zeroth level while bringing a new electron from the valence band to the conduction band, as represented by the third term on the right-hand side of Eq. (4a). Recombination at the rate γ_r is also included across all energy levels.

By combining Eqs. (3) and (4), it is easily shown that MRE is equivalent to the following rate equation:

$$\frac{d\rho}{dt} = \nu_{fi}\rho_u + \gamma_u\rho_k - \gamma_r\rho, \quad (5)$$

which is identical to SRE [see Eq. (1)], except for the second term, associated with CI. In SRE, the CI rate is proportional to the total charge carrier density ρ , whereas in MRE it is proportional to the upper-level population ρ_k , which quantifies the fraction of electrons whose kinetic energy is greater than the critical energy \mathcal{E}_c . Since CI can only occur after the first

electrons have absorbed at least k photons, the avalanche sequence (LH-CI) is effectively delayed with respect to FI. We emphasize that this delay, and the relative contribution of avalanche ionization to breakdown, is directly influenced by both the photon absorption rate γ_{th} and the collisional impact rate γ_u . Mathematical expressions for these two parameters are given later in Eqs. (9) and (10), respectively.

III. DYNAMICAL RATE EQUATION MODEL

The development of the MRE model was motivated by the observation in kinetic simulations (see, e.g., Ref. [1]) of sharp density peaks at multiples of the photon energy ($\hbar\omega$, $2\hbar\omega$, $3\hbar\omega$, ...). In these simulations, however, it was also observed that within about 10 fs these peaks quickly broaden and disappear, due to collisions driving the carriers towards an internal thermal equilibrium. Following a different strategy than for MRE, where no thermalization actually takes place, we make the approximation that on a few-laser-cycle time scale, carrier thermalization has progressed enough such that the energy distribution can be approximated by a continuous distribution, instead of a spiky one. This translates into a simplified rate equation model that accounts for the LH process by using only one auxiliary differential equation.

At thermal equilibrium, assuming a Maxwellian distribution, the fraction of electrons $\xi \leq 1$ that have an energy higher than the critical energy \mathcal{E}_c [see Eq. (2)] is calculated analytically as

$$\xi = \frac{\int_{\mathcal{E}_c}^{\infty} \mathcal{E}^{1/2} \exp[-3\mathcal{E}/2\mathcal{E}_{kin}] d\mathcal{E}}{\int_0^{\infty} \mathcal{E}^{1/2} \exp[-3\mathcal{E}/2\mathcal{E}_{kin}] d\mathcal{E}} \quad (6a)$$

$$= \text{erfc}(r) + \frac{2r}{\sqrt{\pi}} \exp(-r^2), \quad (6b)$$

where $r = \sqrt{3\mathcal{E}_c/2\mathcal{E}_{kin}}$. Note that the average kinetic energy \mathcal{E}_{kin} is related to the electron temperature T by the equipartition theorem, i.e., $\mathcal{E}_{kin} = 3k_B T/2$, where k_B is the Boltzmann constant. The corresponding rate equation is readily obtained by replacing ρ_k in Eq. (5) by $\xi\rho$, which gives

$$\frac{d\rho}{dt} = \nu_{fi}\rho_u + \gamma_u\xi\rho - \gamma_r\rho. \quad (7)$$

The other terms, associated with field ionization ($\nu_{fi}\rho_u$) and electron-hole recombination ($\gamma_r\rho$) are left unchanged [compare with Eqs. (1) and (5)].

We emphasize that Eq. (6) is used to track only the tail of the energy distribution that lies beyond \mathcal{E}_c . The use of a classical distribution, instead of Fermi-Dirac, is justified because the electron gas is usually not very dense (typically a few percent of the material density) and hot enough such that $\mathcal{E}_{kin} \gg \mathcal{E}_F$, where \mathcal{E}_F is the Fermi energy. (See also Fig. 2 and accompanying text for further discussion.)

Inspection of Eq. (6b) shows that the fraction ξ , which also defines the CI rate in the second term on the right-hand side of Eq. (7), is parameterized by the average kinetic energy \mathcal{E}_{kin} . The laser-heating process (LH) is thus conveniently introduced by tracking \mathcal{E}_{kin} with the ordinary differential equation that follows (see Appendix C for a formal derivation):

$$\frac{d\mathcal{E}_{kin}}{dt} = \gamma_{th}\hbar\omega - \gamma_u\xi\mathcal{E}_c - \mathcal{E}_{kin} \left[\nu_{fi} \frac{\rho_u}{\rho} + \gamma_u\xi \right]. \quad (8)$$

The first term on the right-hand side is associated with photon absorption at a rate γ_{th} [see also Eqs. (4a)–(4c)]. The second term represents the kinetic energy lost during impact events occurring at a rate $\gamma_u \xi$. The final term (proportional to \mathcal{E}_{kin}) accounts for the variation of the electron population (see, again, Appendix C for details). The use of Eq. (8) to define dynamically the fraction ξ [Eq. (6b)], which in turn modulates the CI rate in Eq. (7)—inspired the name dynamical rate equation (DRE).

Next, in Sec. IV, we show that results obtained with DRE are comparable to those obtained with MRE. However, an advantage of DRE lies in the possibility to track only the mean kinetic energy \mathcal{E}_{kin} [Eq. (8)], instead of the multiple level populations of MRE [Eqs. (4)]. Later in Secs. V and Sec. VI, we will show that this mathematical simplicity offers advantages to extract effective values from experimental data and for large-scale, three-dimensional electromagnetic modeling.

IV. NUMERICAL ANALYSIS OF THE RATE MODELS

In previous sections, we have described three rate-equation models (SRE, MRE, and DRE) that provide a phenomenological description of the temporal evolution of the electron density on a field-cycle-averaged, statistical level. We have shown that they differ only in the way they respectively account for collisional ionization and, in particular, for the underlying laser-heating process. In this section, we compare all three models numerically and provide further insight into DRE.

To assess the respective behavior of the rate models, we have computed the ratio of the electron density due to collisional ionization ρ_{ci} over the total density ρ when a harmonic electric field $\vec{E}(t) = E \cos(\omega t)$ with constant amplitude E is applied. The ratio $\rho_{\text{ci}}/\rho = 0.5$ is often seen as the avalanche turning point where collisional ionization becomes dominant (i.e., when $\rho_{\text{ci}}/\rho > 0.5$, see Ref. [17]). For each model, the laser intensity $I = cn_0 \epsilon_0 E^2 / 2$ (n_0 is the refractive index of the dielectric without ionization) is set accordingly to get $\rho_{\text{ci}}/\rho \simeq 0.5$ after $t = 100$ fs, which thereby defines a reference fluence to reach the avalanche turning point $F_{\text{av}} = I \cdot 100$ fs.

Field ionization (FI) is described with the Keldysh theory [28] for all the rate-equation models (see Appendix A). Improved FI models (see, e.g., Refs. [18,30,30,31]) would do as well. For simplicity, we have neglected recombination ($\gamma_r = 0$) for this comparison (this contribution will be taken into account later when we compare DRE with experimental data).

In presenting the model equations in Secs. II A, II B, and III, an explicit description of the laser heating rate γ_{th} and of the free-electron-to-neutral impact rate γ_u was not given. Assuming an harmonic laser electric field $\vec{E}(t) = E \cos(\omega t)$ as above, the classical Drude model leads to the following expression for the laser-heating rate [see Appendix B]

$$\gamma_{\text{th}} = \frac{\gamma}{\hbar \omega} \frac{q^2 E^2}{2m_e(\gamma^2 + \omega^2)} = \frac{2\gamma}{\hbar \omega} \mathcal{E}_p, \quad (9)$$

where q and m_e are the charge and effective mass of the electron. In Eq. (9), the plasma parameter γ accounts for collisional damping. For collisions between electrons and neutral

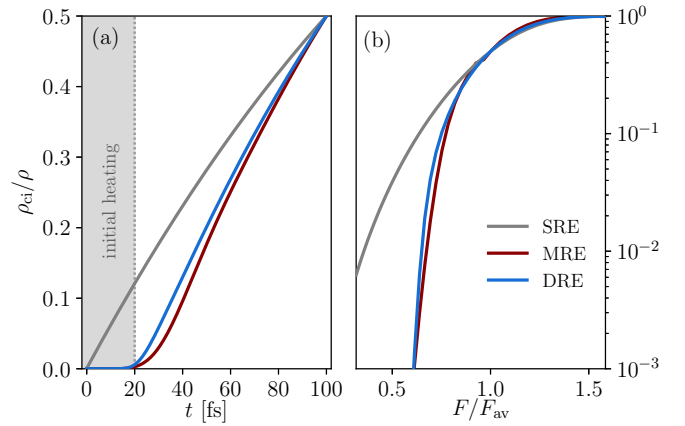


FIG. 1. Relative contribution of collisional ionization (ρ_{ci}) over the global ionization yield ($\rho = \rho_{\text{fi}} + \rho_{\text{ci}}$) obtained with the SRE, MRE, and DRE models. In (a), impact ionization in SRE starts at $t = 0$, while MRE and DRE show an initial time delay needed for the first charge carriers to be heated above the critical energy \mathcal{E}_c . (b) shows that the contribution from impact ionization drops more quickly below the avalanche threshold F_{av} when a laser heating mechanism is included (MRE and DRE). For each model, the fluence F is normalized by the respective F_{av} value ($F_{\text{av}}^{\text{SRE}} = 0.314 \text{ J/cm}^2$, $F_{\text{av}}^{\text{MRE}} = 0.554 \text{ J/cm}^2$, and $F_{\text{av}}^{\text{DRE}} = 0.411 \text{ J/cm}^2$, see text for details). Model parameters are laser wavelength $\lambda = 800$ nm, band gap energy $\mathcal{E}_g = 9$ eV, effective masses $m_e = m_h = m_0$ (with the free electron mass $m_0 = 9.1094 \times 10^{-31}$ kg), material density $\rho_{\text{mat}} = 2 \times 10^{28} \text{ m}^{-3}$, molecular cross section $\sigma_{\text{mat}} = 10^{-19} \text{ m}^2$, linear refractive index $n_0 = 1.5$, recombination rate $\gamma_r = 0$, plasma damping rate $\gamma = 1 \text{ fs}^{-1}$, and impact ionization coefficient (for SRE) $\alpha = 4 \text{ cm}^2/\text{J}$. Electric field strengths E are 3.974 GV/m (SRE), 5.276 GV/m (MRE), and 4.542 GV/m (DRE).

molecules leading to CI, we used the model of Ref. [17], i.e.,

$$\gamma_u = \sigma_{\text{mat}} \rho_u \sqrt{\frac{2\mathcal{E}_{\text{kin}}}{m_e}}, \quad (10)$$

where the subscript u here stands for unionized and σ_{mat} is the material impact cross section. We emphasize that the results obtained with DRE do not change significantly whether we use Eq. (10) or a constant value for the electron-neutral collision rate γ_u . This observation is supported by Ref. [2], where it is shown that the value of γ_u (or that given by the underlying model) has a small influence, as long as it is greater than the plasma heating rate, i.e., if $\gamma_u \gtrsim \gamma_{\text{th}}$.

Numerical results obtained with SRE, MRE, and DRE for a model material whose properties are comparable to SiO_2 are shown in Fig. 1. The similarity between the MRE and DRE results is obvious. Effectively, both predict a transient window of about 20 fs where very few CI events occur, corresponding to the initial heating phase of the first cold electrons brought to the conduction band by FI. In contrast for SRE where LH is neglected, CI starts right away at $t = 0$ regardless of the electron energy, which overestimates systematically the CI contribution. This has a significant impact on the SRE behavior around the avalanche threshold F_{av} . As seen in Fig. 1(b), MRE and DRE effectively predict a sharper transition when approaching F_{av} . Above threshold ($F > F_{\text{av}}$), all three models show a similar trend.

We stress that the initial CI delay observed in Fig. 1(a) does not appear explicitly in the DRE equations. In contrast with other approaches where a constant value is assumed (see, e.g., Refs. [33]), it here follows from the temporal dependence of the impact ionization rate introduced dynamically via Eqs. (6b) and (8). The fact that the DRE results are so close to those of MRE suggests that the plasma thermalization dynamics (e.g., as described by Kaiser *et al.* [1]) has a limited impact on the avalanche process as a whole. We recall that MRE was developed in the limit of an infinite thermalization time, whereas DRE was developed in the limit of an infinitesimal thermalization time. It is thus reasonable to expect that results obtained by solving the internal thermalization dynamics rigorously would lie between DRE and MRE.

To get further insight into the DRE model, we have considered a more realistic scenario where a strong laser pulse is incident on a model material, again similar to SiO₂. The electric field envelope of the laser pulse in vacuum is modeled by a Gaussian function:

$$E_{\text{vac}}(t) = E_0 \exp \left[-2 \ln(2) \left(\frac{t}{\tau} \right)^2 \right], \quad (11)$$

where τ is the full-width at half-maximum (FWHM) duration of the pulse. The laser intensity and fluence in vacuum are then

$$I_{\text{vac}}(t) = c\epsilon_0 |E_{\text{vac}}(t)|^2 = c\epsilon_0 E_0^2 \exp \left[-4 \ln(2) \left(\frac{t}{\tau} \right)^2 \right], \quad (12)$$

and

$$F = \int_{-\infty}^{\infty} I_{\text{vac}}(t) dt = \frac{c\epsilon_0 E_0^2 \tau}{2} \sqrt{\frac{\pi}{\ln(2)}}, \quad (13)$$

respectively.

To account for the reflection of electromagnetic radiation on the sample due to both the intrinsic refractive index n_0 of the material and the laser-induced metallization, we computed the electric field in the bulk with:

$$E_{\text{bulk}}^2(t) = E_{\text{vac}}^2(t) \frac{1-R}{\text{Re}(n)}, \quad (14)$$

where

$$R = \left| \frac{n-1}{n+1} \right|^2 \quad (15)$$

and

$$n^2 = n_0^2 - \frac{\omega_p^2}{\omega^2 + i\omega\gamma}. \quad (16)$$

This last relation is obtained from the Drude model with a plasma frequency $\omega_p^2 = q^2 \rho / \epsilon_0 m_e$, where the value of the electron density ρ is updated dynamically with Eq. (7). As in Eq. (9), γ is the collisional damping rate.

Results obtained with DRE driven by the electric field $E_{\text{bulk}}(t)$ are shown in Fig. 2. For the two presented scenarios ($\tau = 10$ fs, $F = 1.75$ J/cm² and $\tau = 300$ fs, $F = 6.76$ J/cm²), it is observed that at the leading edge of the pulse, most of the plasma comes from FI, as typically expected [see Figs. 2(a) and 2(d)]. However, as electrons get heated up and reach the critical energy \mathcal{E}_c , CI gradually takes over.

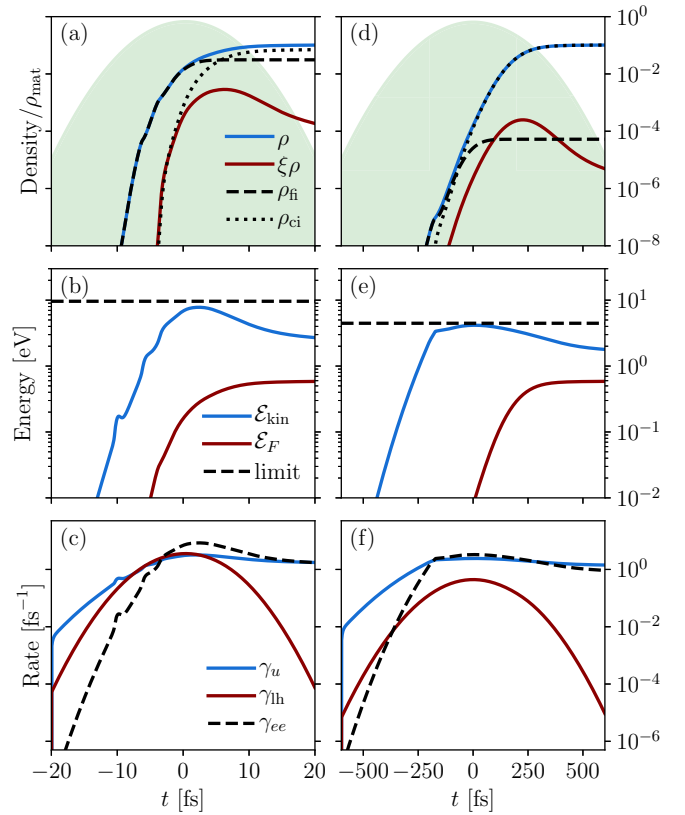


FIG. 2. DRE dynamical details. Left column [(a)–(c)], pulse duration $\tau = 10$ fs and laser fluence $F = 1.75$ J/cm². Right column [(d)–(f)], $\tau = 300$ fs and $F = 6.76$ J/cm². In both cases, the fluence was set to reach 10% of ionized molecules. (a) and (d) show the contribution of FI (ρ_{fi}) and CI (ρ_{ci}) to the total charge density $\rho = \rho_{\text{fi}} + \rho_{\text{ci}}$. The density of electrons with kinetic energy greater than the critical energy \mathcal{E}_c ($\xi\rho$) and the shape of the laser pulse (shaded area) are also shown. In (b) and (e) the kinetic energy of the electron in the conduction band obtained by the numerical integration of Eq. (8) is compared with the Fermi energy (see text) and the upper limit obtained analytically [Eq. (17)]. Finally, in (c) and (f) are shown the electron-neutral collisional rate [γ_u , Eq. (10)] and the photon absorption rate [γ_{lh} , Eq. (9)]. The electron-electron collisional rate [γ_{ee} , Eq. (18)] is not part of the DRE model, but is shown for reference (see text). Parameters are laser wavelength $\lambda = 800$ nm, band gap energy $\mathcal{E}_g = 9$ eV, effective masses $m_e = m_h = m_0$ (with the free electron mass $m_0 = 9.1094 \times 10^{-31}$ kg), material density $\rho_{\text{mat}} = 2 \cdot 10^{28}$ m⁻³, molecular cross section $\sigma_{\text{mat}} = 10^{-19}$ m², linear refractive index $n_0 = 1.5$, recombination rate $\gamma_r = 0$ and plasma damping rate $\gamma = 1$ fs⁻¹.

We compared the average kinetic energy of the electrons \mathcal{E}_{kin} to the Fermi energy $\mathcal{E}_F = \hbar^2 (3\pi^2 \rho)^{2/3} / 2m_e$ and observed that over the entire simulations $\mathcal{E}_{\text{kin}} \gg \mathcal{E}_F$ [see Figs. 2(b) and 2(e)]. This confirms that using a Fermi-Dirac distribution in Eq. (6) would have a negligible influence.

A rough estimate of the upper limit for the average kinetic energy \mathcal{E}_{kin} is obtained in the steady-state regime that follows the initial heating phase and where LH is balanced by the internal energy lost due to CI, i.e., where $\gamma_{\text{lh}} \hbar \omega \simeq \gamma_u \xi \mathcal{E}_c$. For moderate laser intensity, only a small fraction of electrons effectively reach the critical energy such that $\mathcal{E}_{\text{kin}} \ll \mathcal{E}_c$ at all

times. Then, $r \gg 1$ and $\xi \simeq \frac{2r}{\sqrt{\pi}} \exp(-r^2)$ [see Eq. (6b)] such that it is possible, in combination with Eq. (10), to obtain an explicit upper bound:

$$\mathcal{E}_{\text{kin}} < -\frac{3}{2}\mathcal{E}_c \left[\ln \left(\frac{\gamma_{\text{th}} \hbar \omega}{2\mathcal{E}_c \sigma_{\text{mat}} \rho_{\text{mat}}} \sqrt{\frac{m_e \pi}{3\mathcal{E}_c}} \right) \right]^{-1}. \quad (17)$$

This approximation is in good agreement with the numerical results shown in Figs. 2(b) and 2(e) (see dashed lines).

Finally, the laser heating rate γ_{th} and the electron-neutral collision rate γ_u are shown in Figs. 2(c) and 2(f). For comparison, we displayed as well the electron-electron collision rate given by the following formula (see Ref. [6]):

$$\gamma_{ee} = \frac{4\pi\epsilon_0}{q^2} \sqrt{\frac{6}{m_e}} \left(\frac{2\mathcal{E}_{\text{kin}}}{3} \right)^{3/2}. \quad (18)$$

It is then observed that γ_{ee} increases rapidly at the leading edge of the pulse, as the plasma gets initially build up by FI. But after CI takes over FI, the internal collision rate γ_{ee} levels off to around 1 fs^{-1} , which supports the hypothesis of an electronic relaxation time scale at the laser-cycle level. We recall that this observation has motivated the use of a continuous distribution function to develop DRE.

V. EFFECTIVE DRE PARAMETERS FROM EXPERIMENTS

The DRE model presented in Sec. III depends on a closed set of parameters. Some of them can be directly linked to material properties obtained from experimental measurements or *ab initio* calculations (e.g., linear refractive index n_0 , molecular cross section σ_{mat} , etc.). Below we show how effective values for the remaining parameters can be obtained by fitting the DRE model to experimental damage-threshold data.

The laser-induced damage threshold is a common reference to benchmark laser-induced dielectric breakdown models. It is often referred to as the minimum laser fluence F_{th} needed to cause permanent structural modifications to the material. When working on the plasma formation time scale as done here, the damage threshold is often associated with the minimum laser fluence needed to create a plasma density greater than a critical density $\rho \gtrsim \rho_c$ for which the medium becomes opaque to radiation with photon energy $\hbar\omega$. Based on the complex refractive index given at Eq. (16), equating the real and imaginary parts gives the critical density as follows:

$$\rho_c = \left(\frac{\epsilon_0 m_e}{q^2} \right) n_0^2 (\omega^2 + \gamma^2). \quad (19)$$

Alternatively, the total energy deposition was proposed as a better gauge to assess laser-induced damage (see, e.g., Refs. [18,34]). For that matter, we calculate the total energy absorption as

$$\mathcal{E}_{\text{abs}} = \int_{-\infty}^{\infty} [v_{\text{th}} \rho_u \mathcal{E}_g + \rho \gamma_{\text{th}} \hbar \omega] dt, \quad (20)$$

where field ionization events add each \mathcal{E}_g to the total absorbed energy, whereas photon absorption by electrons in the conduction band adds $\hbar\omega$. We emphasize that impact ionization does not contribute globally to the absorbed energy, because it involves only a transfer of energy between electrons. Finally, the damage criterion is defined as the minimal fluence

required for the absorbed energy to be $\mathcal{E}_{\text{abs}} \gtrsim 3 \text{ kJ/cm}^3$, based on values reported in Ref. [34].

TABLE I. Dielectric material parameters associated with the DRE calculations shown in Figs. 3 and 4. Top part of the table are typical values for the linear refractive index n_0 , the band gap \mathcal{E}_g , the material density ρ_{mat} , and the recombination rate γ_r as gathered from Refs. [35,36]. To estimate the molecular cross section σ_{mat} , we have summed the individual cross sections of the constitutive atoms, calculated as the area of a circle with a radius equal to the covalent radius. In the bottom part, one finds the values for the collisional damping rate γ and the effective electron and hole masses m_e and m_h , respectively, extracted from the data. Masses are expressed in units of the free electron mass $m_0 = 9.1094 \times 10^{-31} \text{ kg}$. The fitting procedure is described in the text. Finally, values in parenthesis in the SiO₂ column are those used for Fig. 4, while the value in parentheses for TiO₂ is for the dashed curve in Fig. 3.

	SiO ₂	Al ₂ O ₃	HfO ₂	Ta ₂ O ₅	TiO ₂
n_0	1.45	1.76	2.09	2.1	2.52
\mathcal{E}_g [eV]	9.0	6.5	5.1	3.8	3.3
ρ_{mat} [$10^{28}/\text{m}^3$]	2.20	2.35	2.77	1.12	3.19
σ_{mat} [$10^{-19}/\text{m}^2$]	0.661	1.33	1.24	2.50	1.08
γ_r [ps^{-1}]	4.0	0.0	0.0	0.0	0.0 (1.0)
m_h	1.0 (∞)	1.0	1.0	1.0	1.0
m_e	0.75 (0.8)	0.85	0.7	0.85	0.5
γ [fs^{-1}]	2.0	2.0	2.0	2.0	2.0

First, we compared the results obtained by numerical integration of the DRE model with the experimental data found in Ref. [35]. Computations were done as in Sec. IV. For a given pulse duration τ , the laser fluence F was scanned from 0.1 – 10 J/cm^2 . It was stopped when the total energy absorption \mathcal{E}_{abs} reached 3 kJ/cm^3 (see previous paragraph) and the stop value was identified as the fluence threshold. The same procedure would then be repeated many times for different pulse duration values to build relatively smooth curves.

In Table I, we have listed the numerical values of the DRE parameters used to produce Figs. 3 and 4. Effectively, there are eight of them, but in practice only two are used as free parameters: the plasma damping rate γ and the effective electron mass m_e . Although the effective hole mass m_h has an influence through the reduced mass m_r ; see the expressions for the critical energy \mathcal{E}_c in Eq. (2), the Keldysh rate in Eq. (A1), and the Keldysh parameter in Eq. (A4)]. We find that it is always possible to balance its effect by adjusting γ and m_e . We have thus decided to assign a fixed value to m_h ($m_0 = 9.1094 \times 10^{-31} \text{ kg}$ for Fig. 3 and ∞ for Fig. 4) and perform the adjustment with only γ and m_e . There might be an opportunity to improve DRE by including hole dynamics explicitly in the model and to use the effective hole mass m_h as an extra parameter. However, this is likely to increase the model complexity, as an additional equation similar to Eq. (8) would be needed to track the holes (plus some extra bookkeeping). As it stands, the model already offers more fitting options, e.g., by adjusting the recombination rate γ_r (see, in particular, the dashed curve in Fig. 3, associated with the TiO₂ data).

To optimize the search for the best parameter combination, we have proceeded as follows. First, we set the damping

required for the absorbed energy to be $\mathcal{E}_{\text{abs}} \gtrsim 3 \text{ kJ/cm}^3$, based on values reported in Ref. [34].

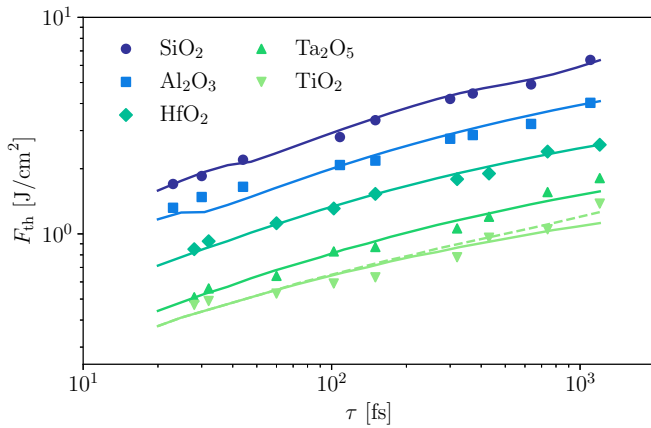


FIG. 3. Comparison between DRE calculations (solid curves) and experimental measurements (shapes) of fluence thresholds F_{th} as a function of pulse duration τ for various dielectric materials. The experimental data sets are from Ref. [35]. The parameters used for the DRE calculations are given in Table I. The dashed line represents an alternative fit for TiO_2 (see text and Table I).

rate γ to adjust the overall scaling trend. Then, the effective mass parameter m_e was chosen to match the height of the corresponding data set. The parameters are not completely independent, however, [see, e.g., Refs. Eq. (19)] and it is sometimes necessary to iterate the procedure. We did not formally assess the quality of the fits, e.g., by minimizing the root-mean-square error. Nevertheless, the computed curves shown in Figs. 3 and 4 do provide compelling evidence that DRE, used with effective parameters, reproduces the global trend of the experimental measurements over several orders

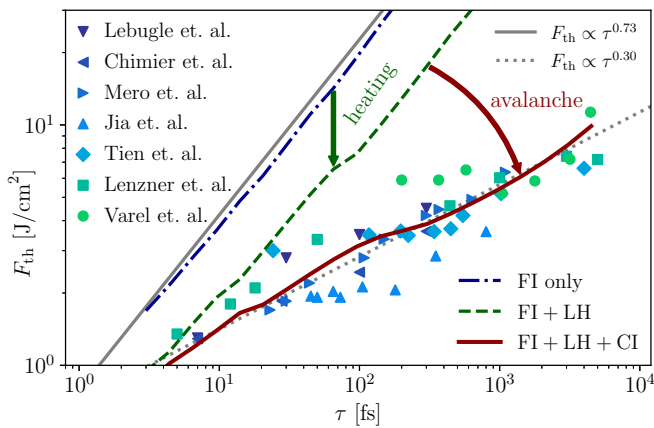


FIG. 4. Laser-induced damage thresholds F_{th} of SiO_2 as a function of pulse duration τ . The experimental data sets from Refs. [7,13,35,38–41] are compared to three different DRE calculations (see also text for details). The blue dash-dotted curve is obtained with field ionization (FI) only [collisional ionization (CI) is turned off by setting the molecular cross section $\sigma_{mat} = 0$] and laser heating (LH) is neglected by using the density criterion [$\rho \gtrsim \rho_c$, see Eq. (19)]. The green dashed curve is obtained with FI, but includes LH by using the energy density criterion [$\mathcal{E}_{abs} \gtrsim 3 \text{ kJ/cm}^3$, see Eq. (20)] (CI is still off with $\sigma_{mat} = 0$). Finally, the red curve is obtained with the full DRE model. Model parameters are given in Table I.

of magnitude of pulse durations and fluence thresholds. We emphasize that proper error assessment should take into account the error margins associated with the experimental data, an information that is not always available in the literature.

The values for material parameters are typically determined by nondestructive measurement methods, where the sample integrity is only slightly perturbed. By definition, assessing the fluence threshold implies driving the material away from the ground state and potentially inducing significant changes to its band structure. The effective values proposed in Table I should therefore be interpreted with care. Note also that effective masses are usually tensors, to account for the anisotropy of the band structure. Simulations with DRE show that the mass parameters have a significant impact on the damage threshold, which in turn suggests that the orientation of the sample with respect to the laser polarization might also play an important role. This effect is likely to be more pronounced in anisotropic crystalline structures. For example, *ab initio* calculations of the electronic band structure of HfO_2 show that the effective masses along the different crystal planes can vary by more than an order of magnitude [37].

Finally, in Fig. 4, we compare DRE with seven experimental data sets for fused silica (SiO_2). Three DRE curves are shown to illustrate the relative contributions from the different parts of the model. First, we have obtained a reasonable agreement with the complete DRE model (FI + LH + CI). The corresponding parameters are given in Table I, with the values in parentheses for the effective masses m_e and m_h . Then we have used these same values, but have removed the CI contribution by setting $\sigma_{mat} = 0$, resulting in the curve labeled “FI + LH”. Finally, for the curve labeled “FI only” there was no CI contribution and we assessed damage using the plasma density criterion [Eq. (19)], which do not properly account for the energy deposition in the material.

Globally, it is observed that the experimental data follow a power-law dependence $F_{th} \propto \tau^\kappa$, with $\kappa \simeq 0.3$. We reproduce this trend using DRE, when both FI and avalanche (LH-CI) are included in the model. When disabling CI, the scaling agreement is systematically lost (then $\kappa \simeq 0.73$). Using the charge density (“FI only”) or the energy deposition (“FI + LH”) does affect the threshold value, but not the scaling trend. Overall, this shows the importance of the entire avalanche sequence (LH-CI) during breakdown for pulse duration under 100 fs. Within the limits of the DRE model, it even suggests that it plays a significant role in the dielectric breakdown process, even for pulse duration down to the 10-fs range. Unfortunately, the cycle-average nature of DRE prevents solid conclusions to be drawn for a shorter pulse duration regime. More on this in the next section.

VI. DISCUSSION

We have presented the DRE model as an alternative to MRE to study the breakdown dynamics in dielectrics induced by femtosecond laser pulses. We have discussed how both models improve upon SRE by dealing explicitly with the gradual heating of the charge carriers by the laser radiation. As a result, charge carriers are created cold and need time to gain enough kinetic energy to trigger collisional ionization.

We have shown that DRE and MRE predict similar delays for the first impact ionization events to occur and for a potential ionization avalanche to unfold.

There are technical advantages for using DRE instead of MRE. First of all, the mathematical simplicity of DRE offers greater flexibility to extract effective values from experimental data. This has been demonstrated by matching the experimental scaling trends for the laser-induced damage threshold of several dielectric materials. Also, we have emphasized that numerical implementation of DRE relies on integrating only two first-order ordinary differential equations, limiting computer memory and CPU requirements to a minimum, e.g., with look-up tables for FI rates and special functions. This offers interesting possibilities for large scale, three-dimensional calculations where computational efficiency is critical. Moreover, in three-dimensional simulations of laser-induced breakdown, e.g., using the finite-difference time-domain (FDTD) or the particle-in-cell (PIC) frameworks, it is common to see high-contrast structures in the plasma density that strongly enhance or suppress the local electromagnetic field (see, e.g., Ref. [42]). This causes significant variations in the local ponderomotive energy and, in turn, of the critical energy for collisional ionization [see Eq. (2)]. For MRE, this implies that numerical convergence is entangled with the number of rate equations that are used. With the original MRE formulation, this number must be chosen beforehand to account for the peak value of the critical energy \mathcal{E}_c over the entire simulation and throughout the material domain. This is an important drawback that should not be overlooked. It was proposed to adjust MRE dynamically [6]. However, special care should be paid for integration in time-domain electromagnetic simulations such as FDTD, as discrete jumps in the numerical calculations can cause severe instability issues. DRE offers a convenient alternative by providing a closed set of equations.

We acknowledge that DRE, as well as the other rate equation models presented above (see also Refs. [2,15]), rely on several approximations and physical simplifications usually accounted for by other popular modeling approaches, e.g., by solving the full set of kinetic Boltzmann equations (see, e.g., Refs. [1,9,11,23]). In particular, rate equations do not account explicitly for several microscopic aspects such as Auger recombination, self-trapping, and phonon coupling that can play significant roles in laser-induced dielectric breakdown. Nevertheless, rate equation models are useful to obtain a phenomenological description of real materials, without the need to introduce all possible contributions in an explicit form, e.g., defects, lattice anisotropy, multibody effects, etc. Rates are then properly interpreted as the effective balance between competing microscopic mechanisms, e.g., collisional ionization versus Auger recombination [9]. To a certain extent, rate equations can be improved to extend their scope, but it should be done with care (see, e.g., Ref. [9] for Auger recombination, [43] for self-trapping and reionization, and [44] for sub-band transitions). We guide the interested reader toward Refs. [3,23] for comparative studies of a rate equation model and the kinetic approach.

We emphasize that DRE does not depend on a specific photoionization or electron-impact cross-section model. It thus appears as a potential test bench. On the one hand,

important progress was made to establish universal FI models, improving on the initial work of Keldysh [28] (see, e.g., Refs. [18,29,31]). On the other hand, kinetic models based on microscopic collision probabilities have helped gain physical insight into the charge carriers dynamics and interactions underlying the ionization avalanche (LH-CI) process (see, e.g., Refs. [1,9,11,15,16]). Testing these FI and LH-CI models within DRE might be useful to identify promising modeling combinations.

Finally, it is important to recall that DRE, like other rate equation models, describe laser-induced breakdown at the field-cycle-averaged level. Studies using DRE with pulse duration below 10 fs should thus be interpreted with some care. In that particular regime, subcycle effects (see, e.g., Refs. [18,45]) and other processes such as photon-assisted avalanche—often referred to as cold ionization avalanche (see, e.g., Ref. [46])—may have a significant impact. More effort is needed to identify whether or not the phenomenology of few-fs pulse effects can actually be captured by DRE, or implemented.

VII. CONCLUSION

In this paper, we have presented a rate-equation model that accounts for the ionization avalanche process phenomenologically by using an auxiliary differential equation to track the gradual heating of the charge carriers. Effectively, this extra equation defines the collisional impact rate dynamically from the fraction of electrons that gained enough energy from the laser field to potentially trigger an ionization avalanche. The computational simplicity of this dynamical rate equation model offers the flexibility to extract effective values from experimental data. This has been shown by matching the experimental scaling trends for the laser-induced damage threshold of several dielectric materials for pulse durations ranging from a few fs to a few ps. Through numerical analysis, we have ascertained that the proposed model gives results comparable to those obtained with multiple rate equations, while offering significant advantages for the development of large-scale, three-dimensional electromagnetic methods for the modeling of laser-induced breakdown in transparent media.

ACKNOWLEDGMENTS

The authors are grateful to two anonymous referees that have greatly contributed to the improvement of the original manuscript. C.V. acknowledges financial support from the Natural Sciences and Engineering Research Council of Canada (NSERC) through the College and Community Innovation Program - Innovation Enhancement Grants (CCIPe 517932-17) and the Fonds de recherche du Québec - Nature et technologies (FRQNT) through the Programme de recherche pour les chercheurs et les chercheuses de collège (2019-CO-254385). L.J.D. was supported by the NSERC Discovery Grant Program and the Sentinel North Program financed by the Canada First Research Excellence Fund.

APPENDIX A: KELDYSH MODEL FOR FIELD IONIZATION IN SOLID-STATE DIELECTRICS

The production rate of electron-hole pairs (in $\text{m}^{-3}\text{s}^{-1}$) induced by a strong laser field $\tilde{E}(t) = E \cos(\omega t)$ in a solid-state dielectric with band gap energy \mathcal{E}_g is given by the Keldysh relation (for details, see Ref. [17], Sec. 2.3.1 and [47], Sec. 2.3)

$$W = \frac{4\omega}{9\pi} \left(\frac{m_r \omega}{\hbar \sqrt{x_1}} \right)^{3/2} \left(\frac{\pi}{2\mathcal{K}(x_2)} \right)^{1/2} \sum_{n=0}^{\infty} e^{-(k+n)\alpha} \Phi(x_3), \quad (\text{A1})$$

where

$$x_1 = \frac{\Gamma^2}{1 + \Gamma^2}; \quad x_2 = \frac{1}{1 + \Gamma^2}; \quad x_3 = \sqrt{\beta(2\nu + n)} \quad (\text{A2})$$

$$\alpha = \pi \frac{\mathcal{K}(x_1) - \mathcal{E}(x_1)}{\mathcal{E}(x_2)}; \quad \beta = \frac{\pi^2}{2\mathcal{K}(x_2)\mathcal{E}(x_2)}; \quad \nu = k - x \quad (\text{A3})$$

$$\Gamma = \frac{\omega \sqrt{m_r \mathcal{E}_g}}{qE}; \quad x = \frac{2}{\pi} \frac{\mathcal{E}(x_2)}{\sqrt{x_1}} \frac{\mathcal{E}_g}{\hbar\omega}; \quad k = \lfloor x + 1 \rfloor \quad (\text{A4})$$

with $\mathcal{K}()$ and $\mathcal{E}()$ being the complete elliptic integrals of the first and second kind, respectively, $\Phi()$ being Dawson's integral, and $\lfloor \dots \rfloor$ denoting the integer part of the argument. To get an FI rate ν_{fi} , the Keldysh density rate W (in $\text{m}^{-3}\text{s}^{-1}$) is divided by the number density ρ_{mat} (in m^{-3}) of the material, resulting in a single-molecule ionization rate $\nu_{\text{fi}} = W/\rho_{\text{mat}}$.

APPENDIX B: DRUDE DESCRIPTION OF THE LASER-PLASMA DYNAMICS

Basic expressions for the ponderomotive energy \mathcal{E}_p and the laser heating (LH) rate γ_{lh} can be derived from the Drude model. At the statistical-continuum level, the instantaneous current $\tilde{i}(t)$ associated with the motion of a charge carrier driven by an electric field $\tilde{E}(t)$ and whose motion is damped by collisions is described by the following equation:

$$\frac{d\tilde{i}(t)}{dt} = -\gamma\tilde{i}(t) + \frac{q^2}{m}\tilde{E}(t), \quad (\text{B1})$$

where fast oscillating variables are marked with a tilde. Parameters q and m are the charge and mass of the charge carrier, respectively. Collisions are included phenomenologically via the damping rate γ .

With $\tilde{E}(t) = E \cos(\omega t)$, the steady-state solution for the single-carrier current is:

$$\tilde{i}(t) = \frac{q^2 E}{m(\gamma^2 + \omega^2)} [\omega \sin(\omega t) + \gamma \cos(\omega t)]. \quad (\text{B2})$$

In turn, the power transferred instantaneously from the laser field to the charge carrier is given by

$$\begin{aligned} \tilde{P}(t) &= \tilde{i}(t) \cdot \tilde{E}(t), \\ &= \frac{q^2 E^2}{m(\gamma^2 + \omega^2)} [\omega \sin(\omega t) \cos(\omega t) + \gamma \cos^2(\omega t)]. \end{aligned} \quad (\text{B3})$$

The two terms in the square brackets are associated with the ponderomotive energy and laser heating, respectively. Both are developed below.

1. Ponderomotive energy

The first term in the square brackets of Eq. (B3) represents a carrier that gains a certain amount of energy during half of an optical cycle, before losing it during the other half, resulting in no net energy gain or loss. This is often referred to as the ponderomotive energy, whose instantaneous expression is given by the integral of the first term in Eq. (B3), such that

$$\begin{aligned} \tilde{\mathcal{E}}_p(t) &= \int q^2 E^2 \frac{\omega \sin(\omega t) \cos(\omega t)}{m(\gamma^2 + \omega^2)} dt, \\ &= \frac{q^2 |\tilde{E}(t)|^2}{2m(\gamma^2 + \omega^2)}. \end{aligned} \quad (\text{B4})$$

In general, the ponderomotive energy is expressed instead in terms of its cycle-averaged expression

$$\mathcal{E}_p = \langle \tilde{\mathcal{E}}_p(t) \rangle = \frac{q^2 E^2}{4m(\gamma^2 + \omega^2)}, \quad (\text{B5})$$

which reduces to the usual, free-particle expression $\mathcal{E}_0 = q^2 E^2 / 4m\omega^2$ in the limit where the plasma damping rate $\gamma = 0$.

2. Laser heating

The last term of Eq. (B3) is associated with the absorption of electrical power from the laser field resulting in a net energy gain after each optical cycle. The rate at which a quantum of light is absorbed is obtained by dividing the last term of Eq. (B3) by the energy of a photon $\hbar\omega$, thus defining an instantaneous laser-heating rate as

$$\tilde{\gamma}_{\text{lh}}(t) = \frac{\gamma}{\hbar\omega} \frac{q^2 |\tilde{E}(t)|^2}{m(\gamma^2 + \omega^2)} = \frac{2\gamma}{\hbar\omega} \tilde{\mathcal{E}}_p(t). \quad (\text{B6})$$

When averaged over a field cycle:

$$\gamma_{\text{lh}} = \langle \tilde{\gamma}_{\text{lh}}(t) \rangle = \frac{\gamma}{\hbar\omega} \frac{q^2 E^2}{2m(\gamma^2 + \omega^2)} = \frac{2\gamma}{\hbar\omega} \mathcal{E}_p. \quad (\text{B7})$$

Insight into the continuum expressions Eqs. (B5) and (B7) obtained from the Drude model is provided in Fig. 5. Optimal

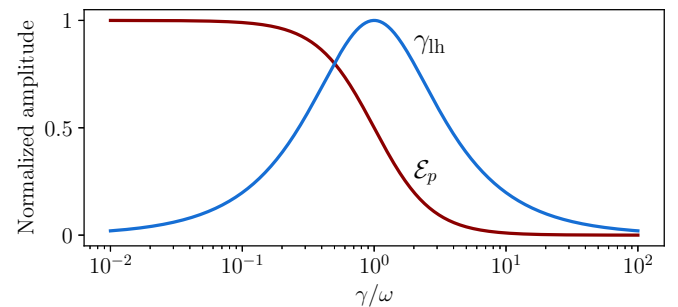


FIG. 5. Insight into the continuum expressions obtained with the Drude model for the ponderomotive energy \mathcal{E}_p [Eq. (B5)] and laser-heating rate γ_{lh} [Eq. (B7)]. Both curves are normalized by their peak amplitudes, \mathcal{E}_0 and \mathcal{E}_0/\hbar , respectively.

heating occurs when the damping rate equals the laser angular frequency, i.e., when $\gamma = \omega$.

APPENDIX C: FORMAL DERIVATION OF THE DRE'S AUXILIARY DIFFERENTIAL EQUATION TO TRACK \mathcal{E}_{kin}

The development of the DRE model is based on the assumption that at thermal equilibrium, the number of carriers with energy \mathcal{E} is given by the following distribution (see Sec. III for discussion):

$$\mathcal{N}(\mathcal{E}) = N \frac{2}{\sqrt{\pi}} \beta^{3/2} \sqrt{\mathcal{E}} e^{-\beta \mathcal{E}}, \quad (\text{C1})$$

where N is the total number of carriers and $\beta = 1/(k_B T)$. The carrier temperature T is related to the average kinetic energy via the equipartition theorem, i.e., $\mathcal{E}_{\text{kin}} = 3k_B T/2$, where k_B is the Boltzmann constant.

The total energy within the carrier gas is thus

$$E_{\text{tot}} = \int_0^\infty \mathcal{E} \mathcal{N}(\mathcal{E}) d\mathcal{E} \quad (\text{C2a})$$

$$= N \frac{2}{\sqrt{\pi}} \beta^{3/2} \int_0^\infty \mathcal{E}^{3/2} e^{-\beta \mathcal{E}} d\mathcal{E} \quad (\text{C2b})$$

$$= N \frac{3}{2} \frac{1}{\beta} \equiv N \mathcal{E}_{\text{kin}}. \quad (\text{C2c})$$

Taking the time derivative of the total energy E_{tot} gives:

$$\frac{dE_{\text{tot}}}{dt} = N \frac{d\mathcal{E}_{\text{kin}}}{dt} + \mathcal{E}_{\text{kin}} \frac{dN}{dt}, \quad (\text{C3})$$

which leads to:

$$\frac{d\mathcal{E}_{\text{kin}}}{dt} = \frac{1}{N} \frac{dE_{\text{tot}}}{dt} - \mathcal{E}_{\text{kin}} \frac{1}{N} \frac{dN}{dt}. \quad (\text{C4})$$

The first term on the right-hand side of Eq. (C4) is associated with the average variation of the total energy within the carrier gas, whereas the second is due to the variation of the carrier population. We get from Eq. (7) that

$$\frac{1}{N} \frac{dN}{dt} \equiv \frac{1}{\rho} \frac{d\rho}{dt} = \nu_{\text{fi}} \frac{\rho_u}{\rho} + \gamma_u \xi - \gamma_r. \quad (\text{C5})$$

Also,

$$\frac{1}{N} \frac{dE_{\text{tot}}}{dt} = \gamma_{\text{th}} \hbar \omega - \gamma_u \xi \mathcal{E}_c - \gamma_r \mathcal{E}_{\text{kin}}, \quad (\text{C6})$$

where the different terms are interpreted as follows. In the first term, a carrier can gain kinetic energy by absorbing a photon of energy $\hbar \omega$ at a rate γ_{th} [see also Eqs. (4)]. The second term is associated with impact ionization occurring at a rate $\gamma_u \xi$, where a hot carrier with kinetic energy greater than the critical energy \mathcal{E}_c [see Eq. (2)] gives away \mathcal{E}_c to bring a new electron to the conduction band (the bottom of the conduction band corresponds to $\mathcal{E} = 0$). The third term describes recombination at a rate γ_r , where an electron with kinetic energy \mathcal{E}_{kin} falls back to the valence band, converting \mathcal{E}_{kin} of energy into radiation or phonon excitation.

Combining Eqs. (C4), (C5), and (C6) gives

$$\frac{d\mathcal{E}_{\text{kin}}}{dt} = \gamma_{\text{th}} \hbar \omega - \gamma_u \xi \mathcal{E}_c - \mathcal{E}_{\text{kin}} \left[\nu_{\text{fi}} \frac{\rho_u}{\rho} + \gamma_u \xi \right]. \quad (\text{C7})$$

Note that the recombination terms cancel out.

-
- [1] A. Kaiser, B. Rethfeld, M. Vicanek, and G. Simon, *Phys. Rev. B* **61**, 11437 (2000).
- [2] B. Rethfeld, *Phys. Rev. Lett.* **92**, 187401 (2004).
- [3] B. Rethfeld, *Phys. Rev. B* **73**, 035101 (2006).
- [4] T. Q. Jia, H. X. Chen, M. Huang, F. L. Zhao, X. X. Li, S. Z. Xu, H. Y. Sun, D. H. Feng, C. B. Li, X. F. Wang, R. X. Li, Z. Z. Xu, X. K. He, and H. Kuroda, *Phys. Rev. B* **73**, 054105 (2006).
- [5] M. Jupé, L. Jensen, A. Melninkaitis, V. Sirutkaitis, and D. Ristau, *Opt. Express* **17**, 12269 (2009).
- [6] B. H. Christensen and P. Balling, *Phys. Rev. B* **79**, 155424 (2009).
- [7] B. Chimier, O. Utéza, N. Sanner, M. Sentis, T. Itina, P. Lassonde, F. Légaré, F. Vidal, and J. C. Kieffer, *Phys. Rev. B* **84**, 094104 (2011).
- [8] X. Jing, Y. Tian, J. Zhang, S. Chen, Y. Jin, J. Shao, and Z. Fan, *Appl. Surf. Sci.* **258**, 4741 (2012).
- [9] N. Brouwer and B. Rethfeld, *J. Opt. Soc. Am. B* **31**, C28 (2014).
- [10] L. Gallais, D.-B. Douti, M. Commandré, G. Batavičiūtė, E. Pupka, M. Ščiuka, L. Smalakys, V. Sirutkaitis, and A. Melninkaitis, *J. Appl. Phys.* **117**, 223103 (2015).
- [11] T. Apostolova, J. Perlado, and A. Rivera, *Nucl. Instr. Meth. Phys. Res. B* **352**, 167 (2015), Proceedings of the 12th International Conference on Computer Simulation of Radiation Effects in Solids, Alacant, Spain, 8–13 June, 2014.
- [12] N. Brouwer and B. Rethfeld, *Phys. Rev. B* **95**, 245139 (2017).
- [13] M. Lebugle, N. Sanner, N. Varkentina, M. Sentis, and O. Utéza, *J. Appl. Phys.* **116**, 063105 (2014).
- [14] S. Guizard, N. Fedorov, A. Mouskeftaras, and S. Klimentov, *AIP Conf. Proc.* **1278**, 336 (2010).
- [15] B. C. Stuart, M. D. Feit, A. M. Rubenchik, B. W. Shore, and M. D. Perry, *Phys. Rev. Lett.* **74**, 2248 (1995).
- [16] N. S. Shcheblanov, E. P. Silaeva, and T. E. Itina, *Appl. Surf. Sci.* **258**, 9417 (2012).
- [17] P. Balling and J. Schou, *Rep. Prog. Phys.* **76**, 036502 (2013).
- [18] P. A. Zhokhov and A. M. Zheltikov, *Sci. Rep.* **8**, 1824 (2018).
- [19] A. Bourgeade, C. Mézel, and O. Saut, *J. Sci. Comput.* **44**, 170 (2010).
- [20] J.-L. Déziel, L. J. Dubé, and C. Varin, Dynamical rate equation model, <https://github.com/cvarin/Dynamical-Rate-Equation-Model>.
- [21] G. Vampa, C. R. McDonald, G. Orlando, D. D. Klug, P. B. Corkum, and T. Brabec, *Phys. Rev. Lett.* **113**, 073901 (2014).
- [22] A. N. Pfeiffer, *J. Phys. B: At., Mol. Opt. Phys.* **53**, 164002 (2020).
- [23] B. C. Stuart, M. D. Feit, S. Herman, A. M. Rubenchik, B. W. Shore, and M. D. Perry, *Phys. Rev. B* **53**, 1749 (1996).
- [24] D. Giguère, G. Olivieri, F. Vidal, S. Toetsch, G. Girard, T. Ozaki, J.-C. Kieffer, O. Nada, and I. Brunette, *J. Opt. Soc. Am. A* **24**, 1562 (2007).

- [25] A. Couairon, E. Brambilla, T. Corti, D. Majus, O. de J. Ramírez-Góngora, and M. Kolesik, *Eur. Phys. J.: Spec. Top.* **199**, 5 (2011).
- [26] M. Kolesik and J. V. Moloney, *Rep. Prog. Phys.* **77**, 016401 (2014).
- [27] C. Varin, G. Bart, T. Fennel, and T. Brabec, *Opt. Mater. Express* **9**, 771 (2019).
- [28] L. V. Keldysh, *Zh. Eksp. Teor. Fiz.* **47**, 1945 (1964) [*Sov. Phys. JETP* **20**, 1307 (1965)].
- [29] V. E. Gruzdev, *Phys. Rev. B* **75**, 205106 (2007).
- [30] P. A. Zhokhov and A. M. Zheltikov, *Phys. Rev. Lett.* **113**, 133903 (2014).
- [31] N. S. Shcheblanov, M. E. Povarnitsyn, P. N. Terekhin, S. Guizard, and A. Couairon, *Phys. Rev. A* **96**, 063410 (2017).
- [32] E. Smetanina, P. González de Alaiza Martínez, I. Thiele, B. Chimier, A. Bourgeade, and G. Duchateau, *Phys. Rev. E* **101**, 063206 (2020).
- [33] A. Vogel, J. Noack, G. Hüttman, and G. Paltauf, *Appl. Phys. B: Lasers Optics* **81**, 1015 (2005).
- [34] S. Guizard, S. Klimentov, A. Mouskeftaras, N. Fedorov, G. Geoffroy, and G. Vilmart, *Appl. Surf. Sci.* **336**, 206 (2015).
- [35] M. Mero, J. Liu, W. Rudolph, D. Ristau, and K. Starke, *Phys. Rev. B* **71**, 115109 (2005).
- [36] E. D. Palik (ed.), *Handbook of Optical Constants of Solids* (Academic Press, Burlington, 1997).
- [37] J. C. Garcia, L. M. R. Scolfaro, J. R. Leite, A. T. Lino, V. N. Freire, G. A. Farias, and E. F. da Silva, *Appl. Phys. Lett.* **85**, 5022 (2004).
- [38] T. Q. Jia, Z. Z. Xu, X. X. Li, R. X. Li, B. Shuai, and F. L. Zhao, *Appl. Phys. Lett.* **82**, 4382 (2003).
- [39] A.-C. Tien, S. Backus, H. Kapteyn, M. Murnane, and G. Mourou, *Phys. Rev. Lett.* **82**, 3883 (1999).
- [40] M. Lenzner, J. Krüger, S. Sartania, Z. Cheng, C. Spielmann, G. Mourou, W. Kautek, and F. Krausz, *Phys. Rev. Lett.* **80**, 4076 (1998).
- [41] H. Varel, D. Ashkenasi, A. Rosenfeld, R. Herrmann, F. Noack, and E. E. B. Campbell, *Appl. Phys. A* **62**, 293 (1996).
- [42] J.-L. Déziel, L. J. Dubé, S. H. Messaddeq, Y. Messaddeq, and C. Varin, *Phys. Rev. B* **97**, 205116 (2018).
- [43] B. Rethfeld, O. Brenk, N. Medvedev, H. Krutsch, and D. H. H. Hoffmann, *Appl. Phys. A* **101**, 19 (2010).
- [44] L. Barilleau, G. Duchateau, B. Chimier, G. Geoffroy, and V. Tikhonchuk, *J. Phys. D* **49**, 485103 (2016).
- [45] C. R. McDonald, G. Vampa, P. B. Corkum, and T. Brabec, *Phys. Rev. Lett.* **118**, 173601 (2017).
- [46] P. P. Rajeev, M. Gertsvolf, P. B. Corkum, and D. M. Rayner, *Phys. Rev. Lett.* **102**, 083001 (2009).
- [47] A. Couairon and A. Mysyrowicz, *Phys. Rep.* **441**, 47 (2007).